Solar Energy 196 (2020) 243–259

Contents lists available at ScienceDirect

Solar Energy

journal homepage: www.elsevier.com/locate/solener

# Diagnostic module for series-connected photovoltaic panels

Martin Garaj[a,*], Kelvin Yiwen Hong[a], Henry Shu-Hung Chung[a], Alan Wai-lun Lo[b], Huai Wang[c]

[a] Department of Electronic Engineering, City University of Hong Kong, Hong Kong
[b] Department of Computer Science, Chu Hai College of Higher Education, Hong Kong
[c] The Faculty of Engineering and Science, Aalborg University, Aalborg, Denmark

ARTICLE INFO

*Keywords:*
Fault diagnosis
Photovoltaic systems
Photovoltaic panels
Evolutionary computation

ABSTRACT

An online diagnostic module for condition monitoring of two series-connected photovoltaic panels is presented. The technique is based on firstly perturbing the terminal voltages and currents of the panels with a switched-inductor circuit, which can also be used for differential power processing, to obtain the large-signal dynamic current-voltage characteristics of the panels. An evolutionary algorithm is used to estimate the intrinsic parameters of the panels from the time series of the sampled panel current and voltage. The conditions of the panels are monitored by observing the long-term changes in the extracted intrinsic parameters. Prototype data acquisition module for studying the conditions of solar panels of different technologies (amorphous and crystalline silicon) with different degrees of damage has been built and evaluated. Results reveal that the estimated intrinsic parameters from large-signal dynamic characteristic correlate with the observed health status of the tested panels. Theoretical predictions are favorably compared with experimental measurements.

## 1. Introduction

The photovoltaic (PV) energy is the fastest growing renewable energy resource for the past several years (Deline et al., 2016). The growing penetration means more grid-connected PV power plants where the efficiency and reliability are the priorities.

The necessity of understanding the risk management in PV power plants has been recognized and studied (Ahadi et al., 2014; Sangwongwanich et al., 2018). In Sangwongwanich et al. (2018), the degradation of PV panels is discussed as complex nonlinear process heavily influenced by local environmental conditions. As discussed in Ahadi et al. (2014), the PV panels are the third most likely cause of the malfunction in PV power generation. Therefore, the ability to evaluate the health status of PV panels in time is a necessary condition for ensuring reliable PV power generation.

PV panel datasheets often include parameters, such as open-circuit voltage, short-circuit current, temperature coefficients and maximum power point. Analytical methods (Humada et al., 2016; Ma et al., 2019; Yahya-Khotbehsara and Shahhoseini, 2018) utilize these parameters to develop lumped models capable of reproducing the voltage-current (I-V) characteristic of PV panel. However, the inevitable degradation process causes deviations in the data provided by the datasheet. Therefore, the data acquisition and underlying analysis needs to be performed on a regular basis.

Conventional data acquisition methods require an acquisition of the static I-V characteristic. This is achieved by slowly varying the operating point of the PV panel while sampling the terminal voltage and current. This process is often performed by external devices or by the central inverter, which makes it time consuming and affects the power generation process.

In Cotfas et al. (2016) and Panigrahi et al. (2016), impedance spectroscopy (IS) is used to acquire AC parameters of PV cells from the dynamic response. The dynamic response can be obtained in a fraction of a second, as the perturbation frequencies are relatively high. However, the method requires an expensive test setup to conduct measurements on disconnected PV cells, thus interrupting power generation.

Differential Power Processing (Qin et al., 2015; Shenoy et al., 2013), as one the latest advancements in boosting the efficiency and reliability of PV power plants, equips the PV string with DC-DC converters parallel to the PV panels. These converters process the power mismatch among the individual panels, enabling the panels to work at their respective Maximum Power Point (MPP). As a direct consequence, the DPP converters can control the operating point of the PV panels.

Altering the control software of the DPP module enables to perturb the terminal voltage of the connected panels at an arbitrary frequency.

* Corresponding author.
*E-mail addresses:* mgaraj2-c@my.cityu.edu.hk (M. Garaj), yiwenhong2-c@my.cityu.edu.hk (K.Y. Hong), eeshc@cityu.edu.hk (H.S.-H. Chung), wllo@chuhai.edu.hk (A.W.-l. Lo), hwa@et.aau.dk (H. Wang).

https://doi.org/10.1016/j.solener.2019.12.019
Received 30 August 2019; Received in revised form 18 November 2019; Accepted 6 December 2019
Available online 17 December 2019
0038-092X/ 

**Nomenclature**

| | |
|---|---|
| $\alpha_{MPP/sc/oc}$ | quantity $\alpha$ at MPP/short-circuit/open-circuit point of I-V char |
| $B_{\text{lim}}$ | maximum number of particles $\theta_B$ |
| $C_k$ | k-th capacitor |
| $C_{sh}$ | junction capacitance |
| $d$ | duty cycle ratio |
| $D$ | averaged duty cycle ratio |
| $D_b$ | bypass diode |
| $\theta$ | chromosome (RJGGA)/particle ($m$-PSO) |
| $\hat{\theta}$ | parent chromosome |
| $\theta_B$ | perturbed particle |
| $\Theta$ | population of chromosomes (RJGGA)/particles ($m$-PSO) |
| $\bar{I}$ | large-signal / filtered (neglecting switching noise) current |
| $I_0$ | reverse saturation current |
| $I_p$ | current measured passing through PV panel |
| $I_{ph}$ | photovoltaic current |
| $J$ | parent pool size |
| $K_{\text{min}}^{(k)}/K_{\text{max}}^{(k)}$ | minimum/maximum of k-th element of$\theta$ |
| $L$ | inductor |
| $M$ | population size |
| $N(\mu, \sigma^2)$ | normal distribution with mean $\mu$ and variance $\sigma^2$ |
| $\eta_c$ | RJGGA parameter of crossover function $\beta(u)$ |
| $\eta_m$ | RJGGA parameter of mutation function $\delta(u)$ |
| $p$ | random number |
| $p_c$ | probability of performing crossover operation |
| $p_j$ | probability of performing jumping operation |
| $p_m$ | probability of performing mutation operation |
| $\varphi^{(k)}$ | k-th element of$\theta$ |
| $\Phi$ | fitness function value |
| $\Phi_c$ | cumulative fitness value |
| $\Phi_r$ | relative fitness value |
| $R_s$ | series resistance |
| $R_{sh}$ | shunt resistance |
| $S_k$ | k-th controlled switch |
| $\bar{V}$ | large-signal/filtered (neglecting switching noise) voltage |
| $V_p$ | voltage measured at PV panel terminals |
| $v_T$ | thermal voltage |

Given shorter acquisition time diminishes the disruption of power generation process, a high frequency is preferable.

At high frequencies, the I-V characteristic exhibits a hysteresis like behavior. This is due to the p-n junction capacitance intrinsic to the material. In Kim et al. (2013) and Suskis and Galkin (2013), a model is proposed based on single-diode static model including a parameter representing the dynamics, adding the capability to reproduce the hysteresis loop.

The estimation of intrinsic parameters can be formulated as an optimization of the model parameters, such that the model's prediction matches the measured terminal voltage and current of perturbed PV panel. The nonlinearity of the model and possibility of multiple local optima makes the problem well suited for evolutionary algorithms.

In Wang et al. (2014) and Askarzadeh and Rezazadeh (2011), a Modified Particle Swarm Optimization ($m$-PSO) is proposed for estimation of intrinsic parameter problems of batteries and fuel-cells, respectively. A regular PSO is an elitist evolutionary algorithm with a shortcoming of possible premature convergence into local optima. The $m$-PSO rectifies the shortcoming by including an additional exploratory action, which enables to "jump out" of local optima, thus potentially preventing premature convergence.

On the other hand, non-elitist evolutionary algorithms possess a greater exploration capability often used in multi-objective optimization for locating Pareto-Optimal front (Deb, 2011). In (Nawaz Ripon et al., 2007), a Real-coded Jumping Gene Genetic Algorithm (RJGGA) is proposed. It is based on common Genetic Algorithm for continuous domain, which has been successfully used in single-objective (Ishibuchi et al., 2006) and multi-objective (Ono et al., 2000) optimization. The RJGGA offers two hyper-parameters, which govern the exploration and exploitation rate.

The novelty of the proposed system for diagnostics of PV panels is the use of DPP hardware to perform the data acquisition within milliseconds, such that it can be performed online, without disconnecting the PV panel. This is achieved by alteration of DPP module's control software, which enables to perform a large-signal voltage perturbation at high-frequencies, where the I-V characteristic exhibits a hysteresis loop. This enables to perform the data acquisition in time period negligible to power generation process and estimate static and dynamic parameters.

The presented work builds on previous work (Garaj et al., 2019), which introduced the concept of DPP modules for data acquisition. The current work extends the method proposed in (Garaj et al., 2019) by studying the impact within a PV string. The results are further extended by experimental verification using solar panels of different technologies in controlled and outdoor conditions.

Furthermore, a comparative convergence study of two quasi-

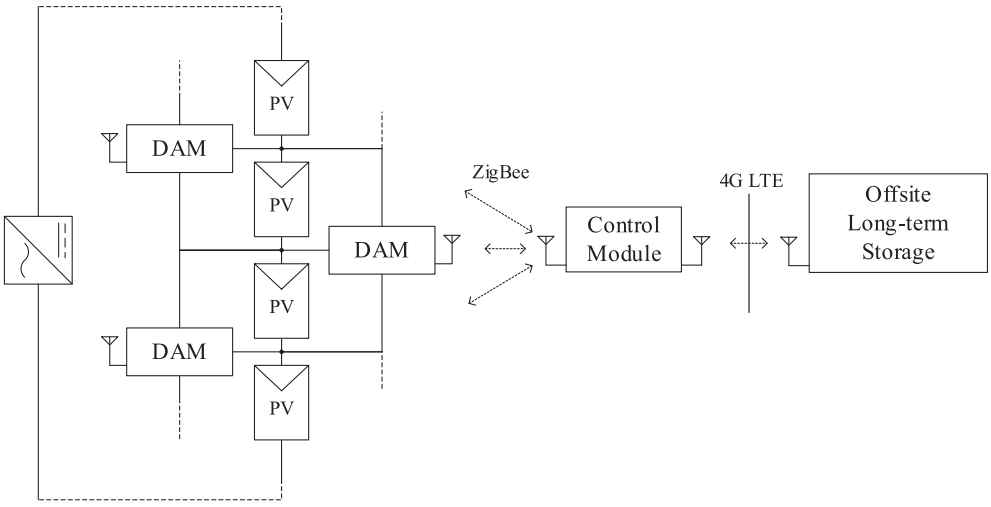


**Fig. 1.** Photovoltaic panel diagnostic system.

random search algorithms, the *m*-PSO and RJGGA, is used to investigate the presence of local optima within the objective function space.

The rest of this paper is organized as follows: In Section 2, the overview of the proposed diagnostic system, hardware of the proposed DPP module for data acquisition and the single-diode dynamic model of a solar panel is introduced. In Section 3, the estimation of intrinsic parameters of a solar panel from the acquired voltage and current time-series is detailed. An analysis of the presence of local optima using *m*-PSO and RJGGA is performed. In Section 4, the performance of the proposed diagnostic system is investigated in simulation and verified by a set of experiments. Finally, Section 5 concludes the major findings.

## 2. Operation of the diagnostic module

A photovoltaic panel diagnostic system for monitoring the condition of two series-connected solar panels is shown in Fig. 1. It consists of three main components, including Data Acquisition Module (DAM), Control Module, and off-site data storage system. The DAM communicates with the control module via ZigBee wireless communication technology and the control module is connected to the data storage system via 4G LTE. Each DAM is connected to two series-connected panels. It firstly perturbs the terminal voltages and currents of the panels with a switched-inductor-based circuit, as shown in Fig. 2, to obtain the large-signal dynamic current-voltage characteristics of the panels and then applies an evolutionary algorithm to estimate the intrinsic parameters of the panels with the time series of the sampled panel voltages and currents.

As shown in Fig. 2, each panel has a bypass diode $D_b$ connected across its terminals for dealing with partial shading condition (Ishaque et al., 2011; Patel and Agarwal, 2008). The switched-inductor circuit consists of two switches, $S_1$ and $S_2$, and an inductor $L$. The capacitors, $C_1$ and $C_2$, provide low-impedance paths for the high-frequency currents generated by the switched-inductor circuit to circulate. $S_1$ and $S_2$ are operated complementarily. The first topology - *Topology 1* with $S_1$ on and $S_2$ off is illustrated in Fig. 3(a). The second topology - *Topology 2* with $S_1$ off and $S_2$ on, is illustrated in Fig. 3(b). For simplicity, $D_b$ is neglected in the following analysis.

In Topology 1,

$$L\frac{di_L}{dt} = v_{P1}, \tag{1}$$

$$C_1\frac{dv_{P1}}{dt} = i_{P1} - i_{string} - i_L, \tag{2}$$

$$C_2\frac{dv_{P2}}{dt} = i_{P2} - i_{string}, \tag{3}$$

where $v_{P1}$ and $v_{P2}$ are the panel voltages of $P_1$ and $P_2$, respectively, $i_{P1}$ and $i_{P2}$ are the panel currents of $P_1$ and $P_2$, respectively, and $i_L$ is the inductor current.

In Topology 2,

$$L\frac{di_L}{dt} = -v_{P2}, \tag{4}$$

$$C_1\frac{dv_{P1}}{dt} = i_{P1} - i_{string}, \tag{5}$$

$$C_2\frac{dv_{P2}}{dt} = i_{P2} - i_{string} + i_L, \tag{6}$$

Let $d$ be the duty cycle of Topology 2 and its average value is $D$,

$$L\frac{d\bar{I}_L}{dt} = (1 - D)\,\bar{V}_{P1} - D\,\bar{V}_{P2}, \tag{7}$$

$$C_1\frac{d\bar{V}_{P1}}{dt} = \bar{I}_{P_1} - \bar{I}_{string} - (1 - D)\,\bar{I}_L \tag{8}$$

$$C_2\frac{d\bar{V}_{P2}}{dt} = \bar{I}_{P_2} - \bar{I}_{string} + D\,\bar{I}_L \tag{9}$$

where $\bar{V}_{P1}$, $\bar{V}_{P2}$, $\bar{I}_{P1}$, $\bar{I}_{P2}$, $\bar{I}_L$ are the averaged values of $v_{P1}$, $v_{P2}$, $i_{P1}$, $i_{P2}$, and $i_L$, respectively, for a given value of $D$.

The relationships between $\bar{V}_{P1}$ and $\bar{I}_{P1}$, and between $\bar{V}_{P2}$ and $\bar{I}_{P2}$ are operating-point- dependent. A dynamic equivalent circuit model of a solar panel (Kim et al., 2013; Suskis and Galkin, 2013) based on single-diode model (Humada et al., 2016; Lim et al., 2015; Silva et al., 2017) is shown in Fig. 4. $\bar{V}_P$ and $\bar{I}_P$ are the averaged values of the panel voltage $v_P$ and panel current $i_P$, respectively. The magnitude of the current source $I_{ph}$ is dependent on the strength of the incident light. The diode $D_{sh}$, junction capacitance $C_{sh}$, and resistor $R_{sh}$ are used to model the p-n junction. The resistor $R_s$ is the series resistance.

The rate of change of $v_{sh}$ is

$$\frac{d\,v_{sh}}{d\,t}(v_{sh},\ \bar{V}_P) = \frac{1}{C_{sh}}\left[I_{ph} - I_o\left(e^{\frac{v_{sh}}{VT}} - 1\right) - \frac{v_{sh}}{R_{sh}} - \frac{v_{sh} - \bar{V}_P}{R_s}\right] \tag{10}$$

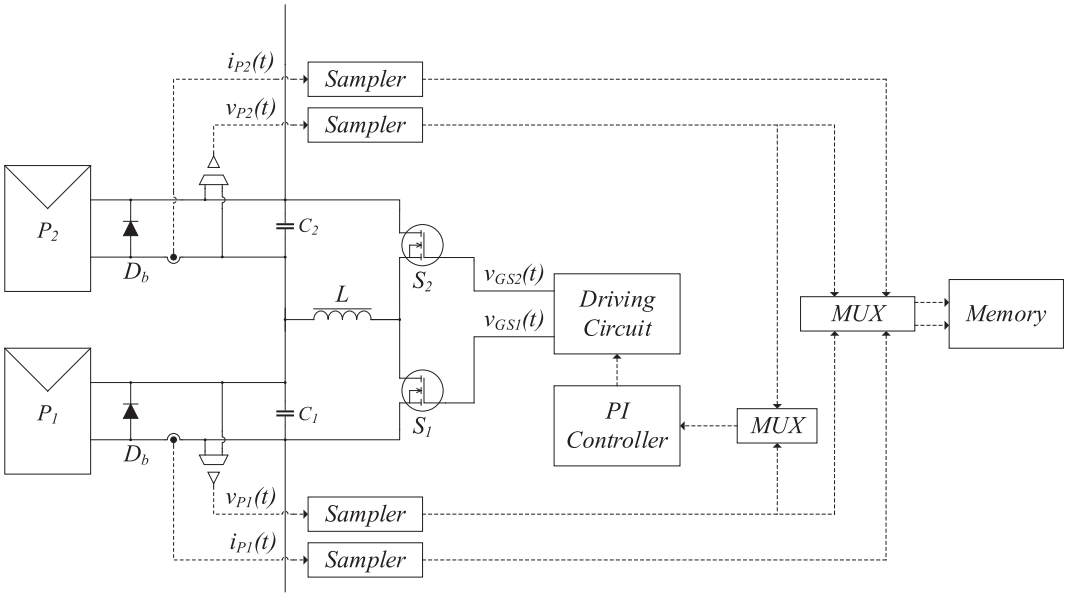


**Fig. 2.** Circuit schematic of the diagnostic module.

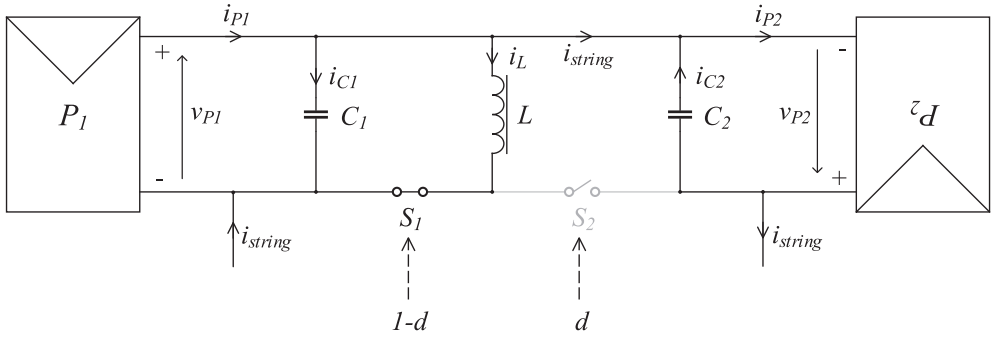


(a) Topology 1.

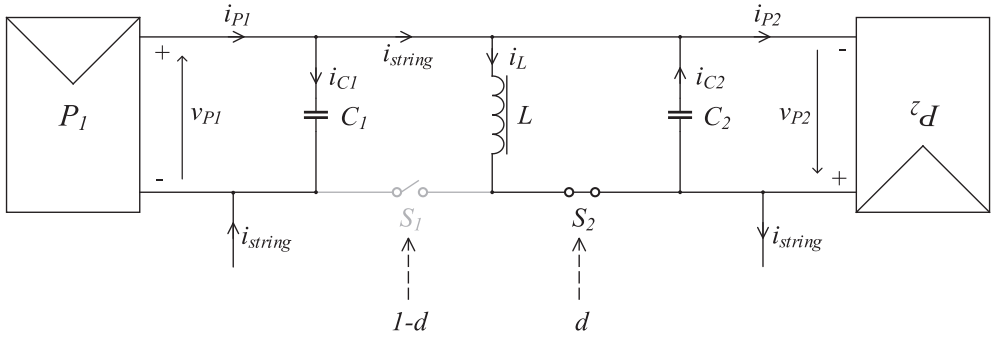


(b) Topology 2.

**Fig. 3.** Equivalent circuit topologies.

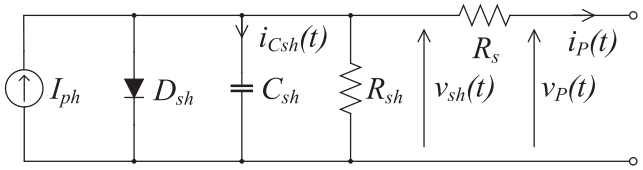


**Fig. 4.** Circuit model of solar panel.

and the panel current $\bar{I}_P$ is

$$\bar{I}_P = \frac{v_{sh} - \bar{V}_P}{R_s} \tag{11}$$

where $I_o$ is the reverse saturation current, and $v_T = n_{id}\, k\, T\, /\, q$, in which $n_{id}$ is ideality factor, $q$ is the electron charge, $k$ is the Boltzmann constant, and $T$ is the temperature of the p-n junction in Kelvin.

Thus, for panel $P_1$, $\bar{V}_P = \bar{V}_{P1}$ and $\bar{I}_P = \bar{I}_{P1}$. For panel $P_2$, $\bar{V}_P = \bar{V}_{P2}$ and $\bar{I}_P = \bar{I}_{P2}$. The characteristics of the panel current ($\bar{I}_P$) – voltage ($\bar{V}_P$) under different values of the excitation frequency $f_o$ and junction

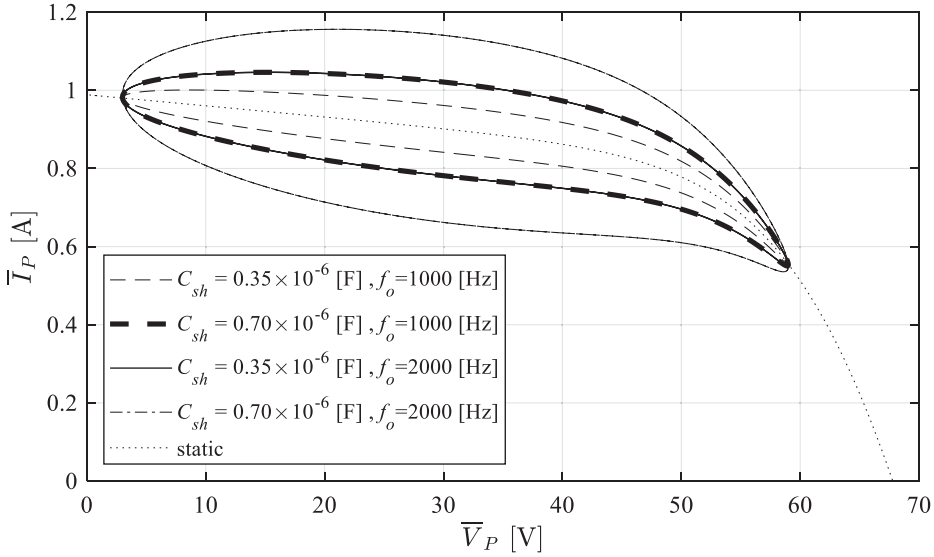


**Fig. 5.** I-V Characteristics of photovoltaic panel.

**Table 1**
Parameters of single-diode dynamic model used in the analysis.

| Param. | Value | Param. | Value |
|---|---|---|---|
| $I_{ph}$ (A) | 1 | $R_{sh}$ (Ω) | 350 |
| I0 (A) | $10 \times 10^{-6}$ | $C_{sh}$ (μF) | 0.350 |
| $v_T$ (V) | 6 | $R_s$ (Ω) | 4 |

capacitance $C_{sh}$ is shown in Fig. 5. The parameters are tabulated in Table 1. The deviation between the static and dynamic characteristics increases with $C_{sh}$ and $f_o$. Thus, if the panel is subject to an AC perturbation, it is crucial to take the effect of $C_{sh}$ into account.

The duty-cycle $D$ is controlled by a proportional-plus-integral (PI) controller with feedback from a voltage sensor of a panel being perturbed. The control action is illustrated by rearranging (7) that

$$D = \frac{\bar{V}_{P1} - L\frac{d\bar{I}_L}{dt}}{\bar{V}_{P1} + \bar{V}_{P2}} \tag{12}$$

It is worth noting that the value of $D$ is predominantly determined by $\bar{V}_{P1}$ and $\bar{V}_{P2}$.

The current-voltage (I-V) trajectories of $P_1$ and $P_2$ when the voltage of the panel $P_1$ is subject to sinusoidal perturbation are shown in Fig. 6. The data for diagnostics is acquired only for the panel following the sinusoidal perturbation, in this case $P_1$. A simulated example of the time-domain waveforms of the voltage and current of the two panels is shown in Fig. 7. Five consecutive time stamps are marked and numbered to relate the time development within the I-V trajectories.

## 3. Estimation of intrinsic parameters with evolutionary algorithm

As panel voltage and current are the only measurable electrical quantities and the equivalent circuit (Fig. 4) is nonlinear in nature, estimation of intrinsic parameters is difficult to be solved in a deterministic way. Previously, *m*-PSO algorithm was used in similar estimation of solar panel intrinsic parameters (Wang et al., 2016), but without performance analysis. The *m*-PSO was also used in other parameter estimation tasks with linear equivalent circuit models (Askarzadeh and Rezazadeh, 2011; Wang et al., 2014), where it successfully managed to estimate the parameters. The motivation to use PSO-based algorithm is its simple implementation, as there are few or none hyper-parameters that require tuning, and its fast convergence,

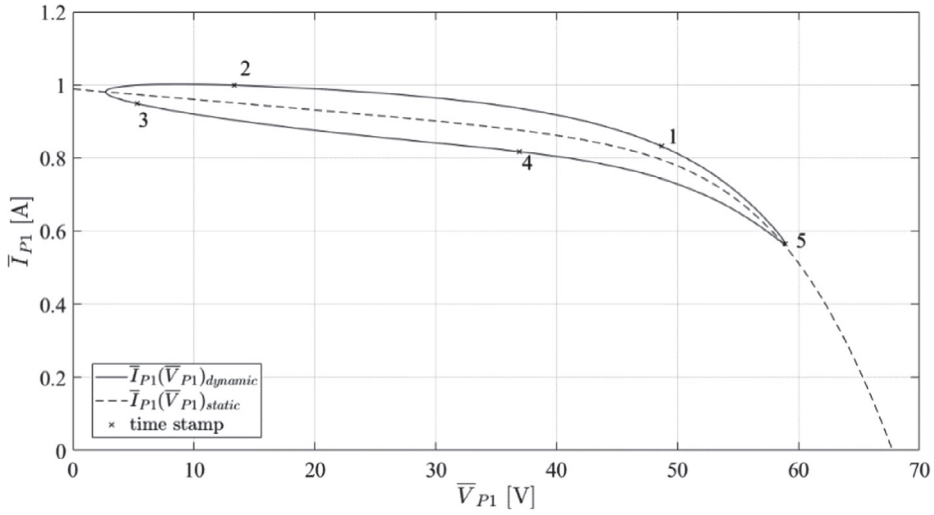


(a) Panel $P_1$.

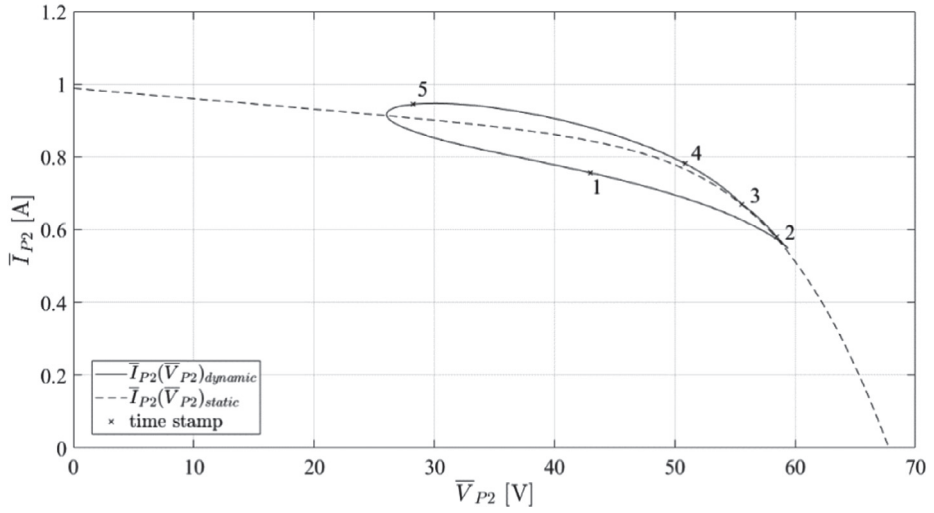


(b) Panel $P_2$.

**Fig. 6.** I-V trajectories of $P_1$ and $P_2$ when the voltage of panel $P_1$ is subject to sinusoidal perturbation.

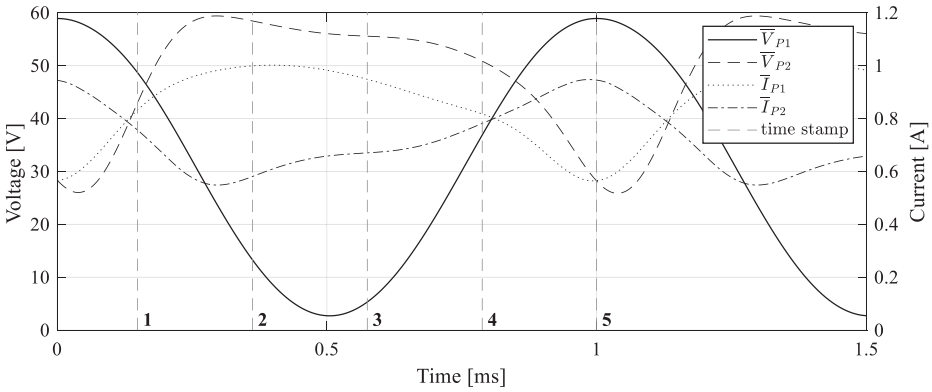


**Fig. 7.** Voltage and current waveforms of $P_1$ and $P_2$ panel throughout the perturbation process.

due to being an elitist kind of algorithm, designed for single-objective optimization.

On the other hand, the RJGGA is a non-elitist algorithm, often used but not limited to multi-objective optimization. The RJGGA has 2 hyper-parameters that govern the ratio of *exploration* and *exploitation*. In the following, a detailed implementation of RJGGA is introduced. A sweep of the 2 hyper-parameters is performed to investigate the effect of the exploration and exploitation rate on the problem of parameter estimation of nonlinear model from measured time series. Furthermore, the implementation of *m*-PSO is mentioned and its performance is used to evaluate and illustrate the presence of local optima.

### 3.1. Optimization mechanism of RJGGA

The RJGGA operates on a set of potential solutions called *population*. Each individual in the population is called *chromosome*. Each chromosome comprises dimensions, which are called *genes*. The quality (fitness) of each chromosome is measured by a *fitness value*, which is determined by a predefined *fitness function*. A new population of potential solutions is generated by performing some selection techniques with individuals having high fitness values getting higher chances of being selected for the reproduction operations, including *mutation* and *crossover*. New generations are produced iteratively until a predefined convergence criterion is reached.

In the following sections, the chromosome and population structures, fitness function, reproduction operations are firstly defined and then the steps of estimating the intrinsic parameters are outlined.

### 3.2. Chromosome and population structures

The parameter set $G$ for each panel is defined as

$$G = \{I_{ph},\ I_o,\ v_T,\ R_{sh},\ C_{sh},\ R_s\}. \tag{13}$$

The (13) forms a basic structure for chromosome $\theta = \{\varphi^{(1)}, \dots, \varphi^{(6)}, \Phi\}$, where the subset $\{\varphi^{(1)}, \dots, \varphi^{(6)}\} = \{I_{ph},\ I_o,\ v_T,\ R_{sh},\ C_{sh},\ R_s\}$ and $\Phi$ is the fitness value of that chromosome. Elements of $\theta$ are bounded, such that $\varphi^{(k)} \in [K^{(k)}_{\min}, K^{(k)}_{\max}]$, where $K^{(k)}_{\min}$, $K^{(k)}_{\max}$ are real numbers, setting the limits of the space, searched for potential solutions.

A group of chromosomes form a population $\Theta$ of size $M$. That is,

$$\Theta = \{\theta[0],\ \theta[1],\ \dots\ \theta[m],\ \dots\ \theta[M-1]\}. \tag{14}$$

### 3.3. Fitness function

The intrinsic parameter estimation process is shown in Fig. 8. The intrinsic parameters are estimated by using the time series of the measured samples of $v_{P1}$, $v_{P2}$, $i_{P1}$, and $i_{P2}$. The intrinsic parameters are estimated from the time series of the panel following the sinusoidal perturbation. If the panel $P_1$ is being perturbed, $v_P = v_{P1}$ and $i_P = i_{P1}$, if the panel $P_2$ is being perturbed, $v_P = v_{P2}$ and $i_P = i_{P2}$.

As the results show, the high-frequency switching noise does not contribute to the large signal dynamics described by the equivalent circuit model. Therefore, $v_P$ and $i_P$ are passed through a low-pass filter to obtain the time series, $\bar{V}_P$ and $\bar{I}_P$, as

$$\bar{V}_P = \{\bar{v}_P[0],\ \bar{v}_P[1],\ \dots\ \bar{v}_P[k],\ \dots\ \bar{v}_P[N-1]\}, \tag{15}$$

$$\bar{I}_P = \{\bar{i}_P[0],\ \bar{i}_P[1],\ \dots\ \bar{i}_P[k],\ \dots\ \bar{i}_P[N-1]\}. \tag{16}$$

Let $V_{sh}$ be the time series of the voltage across $C_{sh}$

$$V_{sh} = \{v_{sh}[0],\ v_{sh}[1],\ \dots\ v_{sh}[k],\ \dots\ v_{sh}[N-1]\}. \tag{17}$$

Let $I_{pred}$ be the time series of the panel current predicted by the Panel Current Predictor (PCP) with $\bar{V}_P$ as the input

$$I_{pred} = \{i_{pred}[0],\ i_{pred}[1],\ \dots\ i_{pred}[k],\ \dots\ i_{pred}[N-1]\}. \tag{18}$$

The time series of the predicted panel current is calculated by a PCP with the intrinsic parameter estimated by the RJGGA and the time series of the actual panel voltage. Each predicted value in the series, i.e. $i_{pred}[k]$ in (18) is calculated by the following four steps:

*Step (1)* For $k = 0$, the rate of change of $v_{sh}$ is assumed to be zero. Thus,

$$\frac{d\,v_{sh}}{d\,t}(v_{sh},\ \bar{v}_P) = 0. \tag{19}$$

Based on (10),

$$I_{ph} = I_o\,(e^{\frac{v_{sh}[0]}{v_T}} - 1) + \frac{v_{sh}[0]}{R_{sh}} + \frac{v_{sh}[0] - \bar{v}_P[0]}{R_s}. \tag{20}$$

*Step (2)* Based on (11), the predicted value of $i_{pred}[k]$ is

$$i_{pred}[k] = \frac{v_{sh}[k] - \bar{v}_P[k]}{R_s}. \tag{21}$$

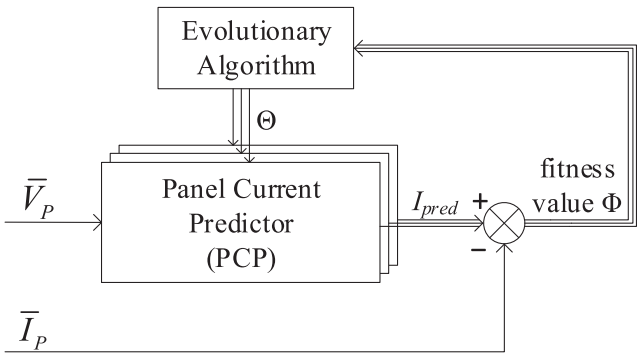


**Fig. 8.** Mechanism of the parameter estimation process.

*Step (3)* $v_{sh}$ is updated by using trapezoidal rule with the formula of

$$v_{sh}[k+1] = \frac{h}{2}\left(\frac{dv_{sh}}{dt}(v_{sh}[k+1], \bar{v}_P[k+1]) + \frac{dv_{sh}}{dt}(v_{sh}[k], \bar{v}_P[k])\right) - v_{sh}[k]. \tag{22}$$

where $h$ is the step size equal to the sample period and the $\frac{dv_{sh}}{dt}(\cdot)$ is defined in (10). Eq. (22) is solved by Newton-Raphson method.

*Step (4)* $k = k + 1$ and the process will go to Step 2 again until $k = N - 1$.

The fitness of each chromosome $\theta$ in each generation *gen* is measured by a fitness value $\Phi$ – an index of merit. It is defined as

$$\Phi(\theta[m], gen) = \left(\frac{1}{N_2 - N_1 - 1}\sum_{k=N_1}^{N_2}(i_{pred}[k] - \bar{i}_P[k])^2\right)^{-1}, \tag{23}$$

where $N_1$ and $N_2$ define the start and end samples, respectively, of the time series in calculating $\Phi$.

### 3.4. Reproduction operations

Reproduction operations, crossover and mutation, evolve the chromosomes over generations within the search space. The reproduction process is in part guided by the fitness value $\Phi$ and in part random, resulting in quasi-random search.

The two reproduction operations are described as follows.

#### 3.4.1. Crossover operation

The crossover operation produces two offspring chromosomes, $\theta_1 = \{\varphi_1^{(1)}, \dots, \varphi_1^{(6)}\}$ and, $\theta_2 = \{\varphi_2^{(1)}, \dots, \varphi_2^{(6)}\}$from two parents, $\hat{\theta}_1 = \{\hat{\varphi}_1^{(1)}, \dots, \hat{\varphi}_1^{(6)}\}$ and $\hat{\theta}_2 = \{\hat{\varphi}_2^{(1)}, \dots, \hat{\varphi}_2^{(6)}\}$ with the formula of

$$\varphi_1^{(i)} = \frac{1}{2}[(1-\beta^{(i)})\hat{\varphi}_1^{(i)} + (1+\beta^{(i)})\hat{\varphi}_2^{(i)}], \tag{24}$$

$$\varphi_2^{(i)} = \frac{1}{2}[(1+\beta^{(i)})\hat{\varphi}_1^{(i)} + (1-\beta^{(i)})\hat{\varphi}_2^{(i)}], \tag{25}$$

where $i = [1, 2, \dots, 6]$.

$\beta^{(i)}$ is defined as

$$\beta^{(i)}(u) = \begin{cases} (2u)^{\frac{1}{\eta_c+1}} & \text{if } u \leqslant 0.5 \\ [2(1-u)]^{-\frac{1}{\eta_c+1}} & \text{Otherwise} \end{cases} \tag{26}$$

where $u \in [0, 1]$ is a random number.

The function of $\beta^{(i)}(u)$ with respect to the value of $\eta_c$ is shown in Fig. 9(a). Based on (24)–(26), the larger the value of $\beta^{(i)}(u)$ the higher the probability of obtaining offspring chromosomes further from parents. Conversely, if $\beta^{(i)}(u)$ is close to unity, offspring chromosomes are created close to parent chromosomes. Therefore, the variation of the parameter $\eta_c$ of the function $\beta^{(i)}(u)$ changes the rate of exploration and exploitation (Crepinsek et al., 2011), as illustrated in Fig. 9(a).

#### 3.4.2. Mutation operation

The mutation operation produces an offspring chromosome $\theta = \{\varphi^{(1)}, \dots, \varphi^{(6)}\}$ from one parent $\hat{\theta} = \{\hat{\varphi}^{(1)}, \dots, \hat{\varphi}^{(6)}\}$ through replacing the value of a single dimension $\varphi^{(k)}$ with the value of

$$\varphi^{(k)} = \hat{\varphi}^{(k)} + (K_{MAX}^{(k)} - K_{MIN}^{(k)})\,\delta, \tag{27}$$

where $k \in \{1, 2, \dots, 6\}$ is selected randomly.

The value of $\delta$ is defined as

$$\delta(u) = \begin{cases} (2u)^{\frac{1}{\eta_m+1}} - 1 & \text{if } u \leqslant 0.5 \\ 1 - [2(1-u)]^{-\frac{1}{\eta_m+1}} & \text{Otherwise} \end{cases} \tag{28}$$

where $u \in [0, 1]$ is a random number.

Based on (27) and (28), if the value of $\delta$ is far from zero, offspring chromosome is created far away from the parent chromosome. Conversely, if $\delta$ is close to zero, the offspring chromosome will be close to the parent chromosomes. Therefore, the parameter $\eta_m$ of the function $\delta(u)$ relates the mutation operation and the rate of exploration and exploitation. The function of $\delta(u)$ with respect to the value of $\eta_m$ is shown in Fig. 9(b).

Both crossover and mutation operations are related to the rate of exploration and exploitation through the respective parameters $\eta_c$ and $\eta_m$. The major difference between crossover and mutation operation is the direction, in which the search space is explored and/or exploited. The crossover creates offspring chromosomes in direction irrespective of the base coordinate system (alters all genes in a chromosome), while the mutation mostly creates offspring chromosomes along single dimension (altering single gene in a chromosome).

### 3.5. Steps of estimating intrinsic parameters

With the help of Fig. 10, the following steps are performed in each generation

#### 3.5.1. Initialization

The RJGGA starts with initializing the population size ($M$), size of parent pool ($J$), maximum number of generations ($gen_{\max}$), probability of performing jumping operation ($p_j$), probability of performing crossover operation ($p_c$), probability of performing mutation operation ($p_m$), and setting the generation counter (*gen*) to zero. The parameters in all chromosomes are randomly initialized with the values lying within the corresponding design limits. By using the method described in Section 3.3, the fitness values of all chromosomes are calculated.

The population size $M$ is chosen by considering the search dimension. As suggested in (Nawaz Ripon et al., 2007), $J = 25$ and $M = 125$, which yields 100 offspring chromosomes in every generation. The adaption of the probabilities $p_c$ and $p_m$ can be classified into several approaches, including static, dynamic deterministic, dynamic adaptive, and dynamic self-adaptive (Srinivas and Patnaik, 1994). The static

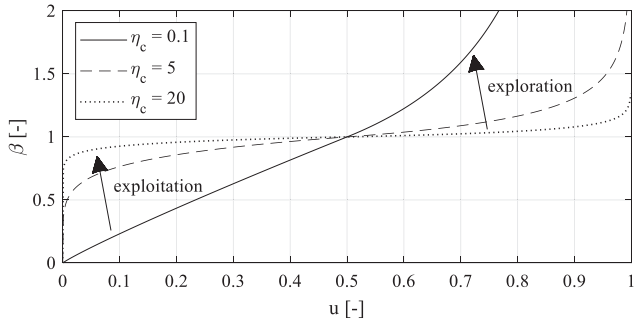


(a) Crossover $\beta(u)$ function.

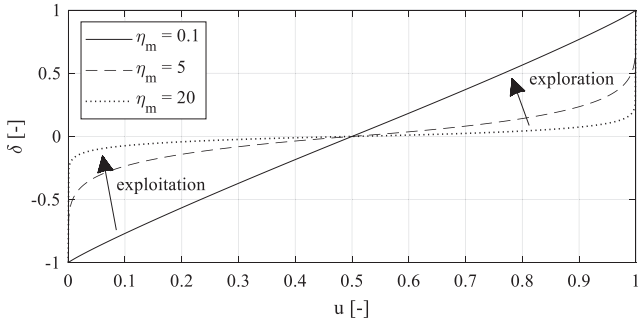


(b) Mutation $\delta(u)$ function.

**Fig. 9.** Functions governing the impact of crossover and mutation operations.

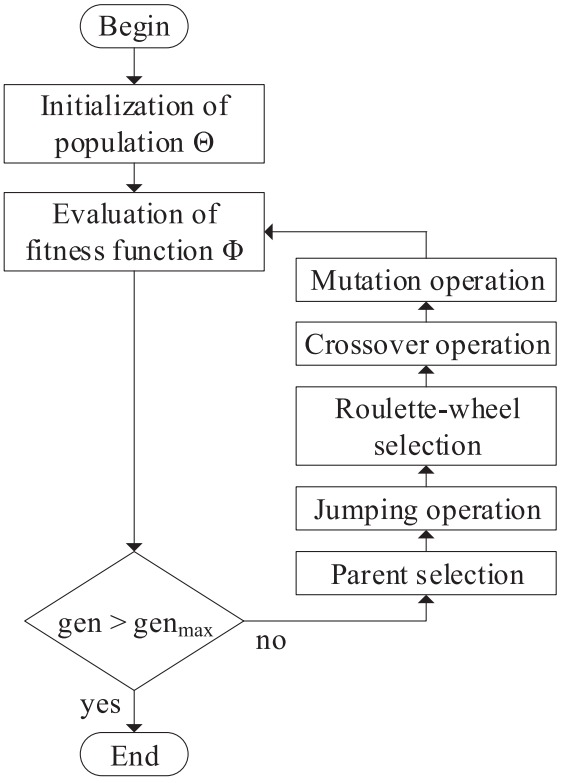


**Fig. 10.** Flowchart of RJGGA.

approach with $p_c$ and $p_m$ fixed throughout the evolution is adopted, to clearly relate the $\eta_c$ and $\eta_m$ with exploration and exploitation rate. As discussed in (Nawaz Ripon et al., 2007), the recommended values for $p_c$, $p_m$, and $p_j$ are 0.9, 0.01, and 0.15, respectively.

#### 3.5.2. Formation of parent pool

A parent pool is formed by choosing first $J$ chromosomes with the highest fitness value in the population pool. Hence, $J < M$.

#### 3.5.3. Jumping operation

Every parent has a chance $p_j$ to enter into a jumping operation. Once the parent is selected, an additional parent is selected randomly. If the two parents are the same, mutation operation will be performed. If the parents are different, crossover operation will be performed. The new individuals are inserted back to the parent pool to replace the original parents.

#### 3.5.4. Selection process for crossover or mutation operation

Based on the roulette wheel rule, a selection process is performed. It starts with the calculation of the fitness value $\Phi(\theta[m],\ gen)$ with (23), relative fitness value $\Phi_r(\theta[m],\ gen)$, and the cumulative fitness value $\Phi_c(\theta[m],\ gen)$ for chromosome $\theta[m]$, which are defined as

$$\Phi_r(\theta[m],\ gen) = \frac{\Phi(\theta[m],\ gen)}{\sum_{m=0}^{M-1}\Phi(\theta[m],\ gen)}, \tag{30}$$

$$\Phi_c(\theta[m],\ gen) = \sum_{z=1}^{m}\Phi_r(\theta[z],\ gen). \tag{31}$$

A random number $p \in [0,\ 1]$ is generated and compared with $\Phi_c(\theta[m],\ gen)$, $\forall m = [0,\ 2,\ \ldots,\ M-1]$. If $\Phi_c(\theta[m-1],\ gen) < p < \Phi_c(\theta[m],\ gen)$, $\theta[m]$ is selected to conduct crossover or mutation operation. Chromosomes having higher fitness values will have higher probability to survive and might appear repeatedly in the new population.

#### 3.5.5. Crossover and mutation operations

The chromosomes selected by the roulette wheel are considered for crossover and mutation operation. To determine whether a chromosome will undergo crossover operation, a random selection test (RST) is executed. A random number $p \in [0,\ 1]$ is generated and compared with $p_c$. If $p < p_c$, the chromosome is selected. Another chromosome is chosen by the same procedure for the crossover operation as described in Section 3.4.1.

The mutation operation, as described in Section 3.4.2, also starts with an RST. A random number $p \in [0,\ 1]$ is generated and compared with $p_m$. If $p < p_m$, the gene is selected for mutation. A random number will be generated for the chosen gene with a value within the parameter limits, $[K_{\min}^{(k)},\ K_{\max}^{(k)}]$, as described in Section 3.2.

The offspring chromosomes generated by the crossover and mutation operations are added into the population pool. The two operations are repeated until $(M-J)$ offspring chromosomes are produced.

### 3.6. RJGGA hyper-parameters

The exploration and exploitation rates of the RJGGA are governed by (26) and (28), determined by $\eta_c$ and $\eta_m$, respectively. The sweep is performed for $\eta_c = \{0.1,\ 5,\ 20\}$ and $\eta_m = \{0.1,\ 5,\ 20\}$. Fig. 11(a)–(i) shows the convergence curves for ten initial populations with different values of $\eta_c$ and $\eta_m$.

The following trends can be observed from the convergence curves in Fig. 11(a)–(i):

- parameter $\eta_c$ is inversely related to the rate of convergence
- parameter $\eta_m$ is inversely related to the number of sudden jumps, presented as steps in the convergence curve

To achieve efficient utilization of computational resources, a consistent convergence rate yielding a consistent set of final solutions (despite different initialization) is desired. This is observed in the Fig. 11 (a) when the $\eta_c = 0.1$ and $\eta_m = 20$. These values correspond to the exploration of the search space using crossover while the mutation plays role in exploitation (Nawaz Ripon et al., 2007).

### 3.7. Optimization mechanism of m-PSO

Fig. 12 illustrates an execution flow of the $m$-PSO algorithm implemented according to Wang et al. (2016).

The fitness value $\Phi$ evaluation in Section 3.3 and the optimization procedure illustrated in Fig. 8 are the same as in the implementation of RJGGA. In the following, only the highlighted part is described, corresponding to the modification of general PSO, which describes a mechanism to prevent premature convergence into local optima.

The mechanism is based on perturbing the globally best particle $\theta_G$ (*particle* and *chromosome* are used interchangeably among PSO and GA algorithms and follow the definition in Section 3.2), in a random direction $\delta$. The elements of a random vector $\delta^{(i)}$ are generated from a normal distribution $N(\mu, \sigma^2)$ with $\mu = 0$ and given variance $\sigma^2$, such that $\delta^{(i)} \sim N(0,\ \sigma^2)$ for $i = [1,\ \ldots,\ 6]$. The perturbed particles $\theta_B^k$ are generated by

$$\theta_B^k = \theta_G + \frac{2^{k-1}}{2^d}(K_{\max} - K_{\min})\delta, \tag{32}$$

where $d = 6$.

Eq. (32) generates particles $\theta_B^k$ for $k = \{1,\ 2,\ 3,\ \ldots\}$ until any dimension $i$ of $\theta_B^k$ is beyond search limits, such that $\theta_B^{(i)k} \notin [K_{\min}^{(i)},\ K_{\max}^{(i)}]$, or until the predetermined amount $B_{\lim}$of particles $\theta_B$ is reached. If any $\theta_B^{(i)k}$ is beyond search limits before the amount of particles $B_{\lim}$ is reached, the counter $k$ resets, new $\delta$ is generated and the mechanism continues to generate additional particles $\theta_B$, until the $B_{\lim}$ is reached.

To investigate the performance of the $m$-PSO, the variance of the normal distribution generating the elements of $\delta$ is set to $\sigma^2 = 0.1329$,

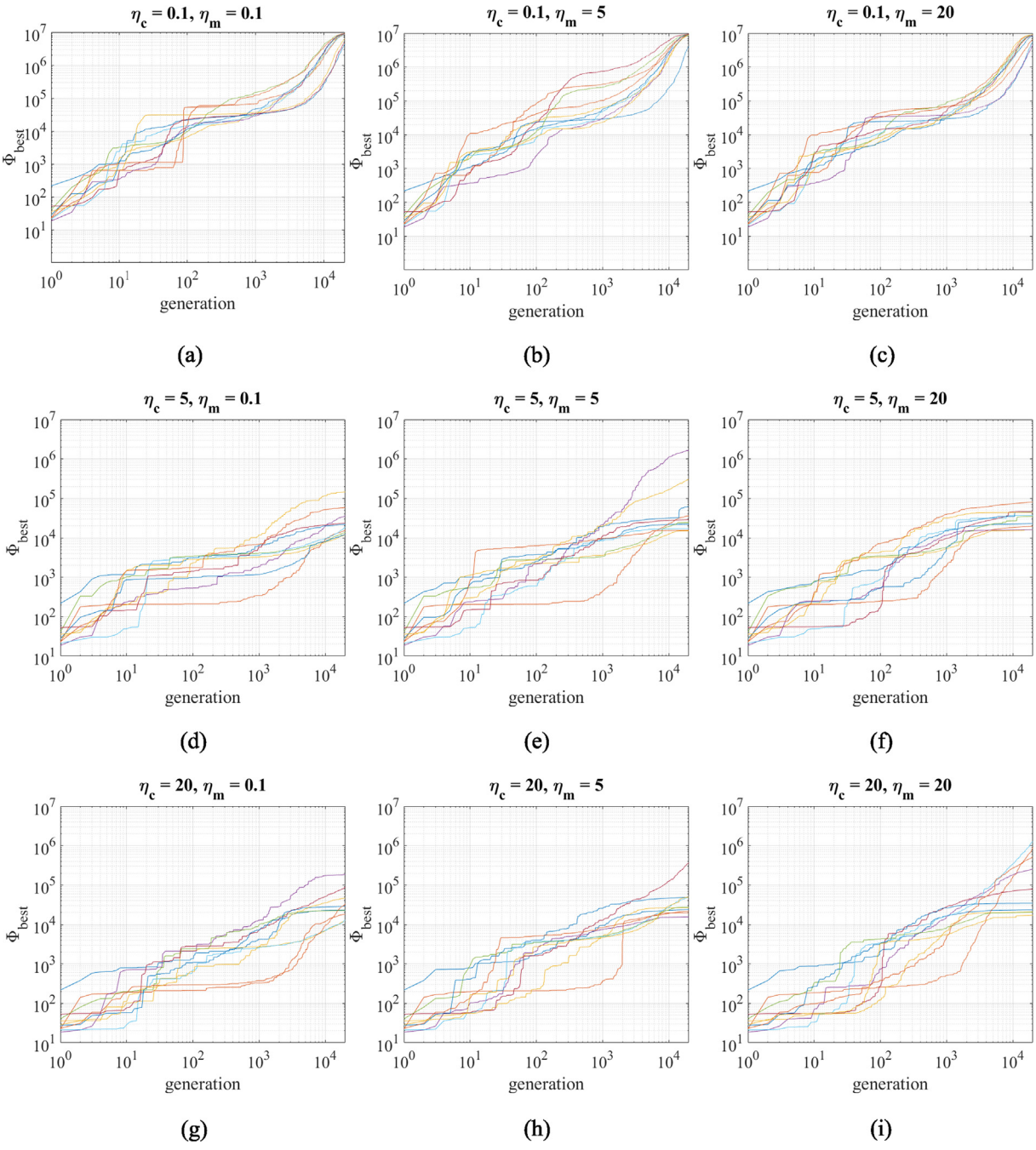


**Fig. 11.** (a)–(i) Convergence curves of RJGGA hyper-parameter sweep.

0.0719 and 0.0362, respectively. These values are obtained by solving

$$p(|N(0, \sigma^2)| < 0.5)^d = P \tag{33}$$

where $d = 6$, $p(\cdot)$ is a probability density function and $P = 33\%$, 68%, and 95%, respectively.

Eq. (33) guarantees that on average, $P$% of the perturbation vectors $\delta$ have elements smaller than half of the search space. This means, with a larger $P$, more particles $\theta_B$ are generated consecutively in the direction of the perturbation vector $\delta$ without reaching the search limits $[K_{\min}, K_{\max}]$, leading to finer exploration. Conversely, a smaller value of $P$ leads to coarser exploration, with $\delta$ getting generated more often.

### 3.8. m-PSO Hyper-parameter

Fig. 13 illustrates the convergence curves for $m$-PSO with population $M = 25$ particles, in accordance with (Wang et al., 2016), and $B_{\lim} = 75$, which equals 100 evaluations of fitness function $\Phi$ per generation, the same as the RJGGA implementation. This ensures the $m$-PSO and RJGGA use similar amount of computational resources.

The red circles in Fig. 13 denote a perturbed particle $\theta_B$ generated by (32), which became globally best particle $\theta_G$ in the following generation.

The following trends can be observed from the convergence curves in Fig. 13(a)–(c):

- Sudden jumps in the convergence curves are related to a mechanism producing particles $\theta_B$.
- Flat regions in the convergence curves are related to the lack of progress within the search, even when significantly better solutions exist, suggesting an existence of local optima.

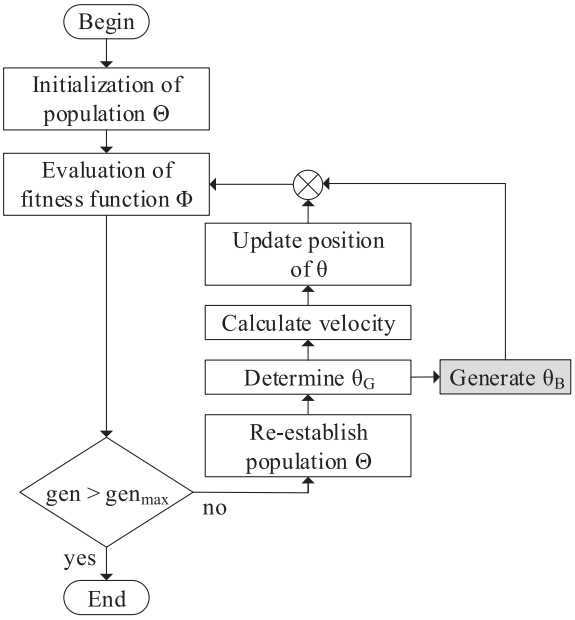


**Fig. 12.** Flowchart of *m*-PSO.

- A trend can be observed where the rate of convergence and the final fitness value correlate with growing value of $P$, suggesting finer exploration is preferable.

## 4. Simulation and experimental results

Since the intrinsic parameters of PV panels cannot be explicitly measured, the proposed diagnostic technique is firstly validated in computer simulation and then experimentally verified with various solar panels under different conditions.

### 4.1. Simulation validation

A simulated setup of a PV string with 6 series connected PV panels, an inverter and the proposed DAM is simulated in PSIM as illustrated in Fig. 14. The inverter is modeled as a resistor and set to drive the string near the MPP, emulating the control strategy of a real inverter. The intrinsic parameters of the PV panels used in simulation are given in Table 1.

The simulation investigates the voltage and current of the PV string, when the $DAM_3$ performs the data acquisition of the panel $P_3$. The voltage and current series of the panels and the inverter before, during and after the perturbation are illustrated in Figs. 15 and 16,

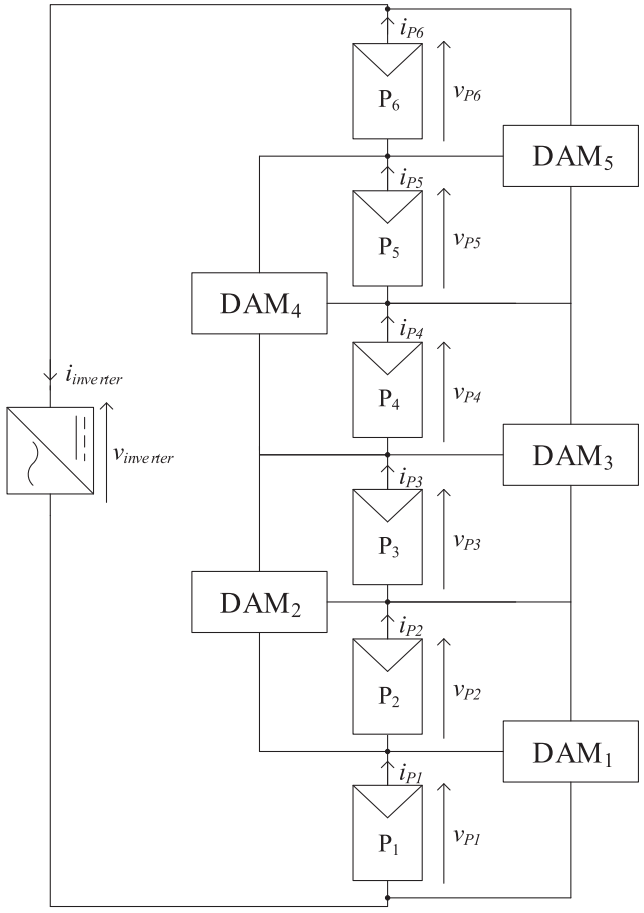


**Fig. 14.** Simulation setup.

respectively.

The DAMs form a regular DPP configuration (Shenoy et al., 2013) and perform DPP control when not performing the diagnostics.

The diagnostic process within the simulation is performed as follows:

- $DAM_3$ is instructed to perform data acquisition from panel $P_3$.
- $DAM_2$ and $DAM_4$ are instructed to curl the control to not interfere with the perturbation process performed by $DAM_3$.
- $DAM_1$ and $DAM_5$ are set to control $P_1$ and $P_6$, respectively, to follow a constant voltage reference.

The $DAM_3$ then induces large signal perturbation between the $P_3$

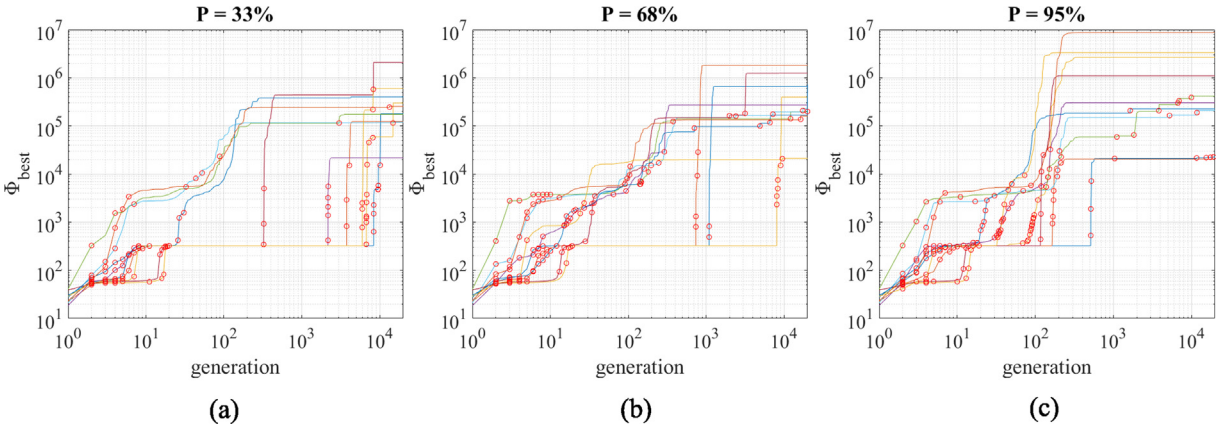


**Fig. 13.** Convergence curves of *m*-PSO hyper-parameter sweep.

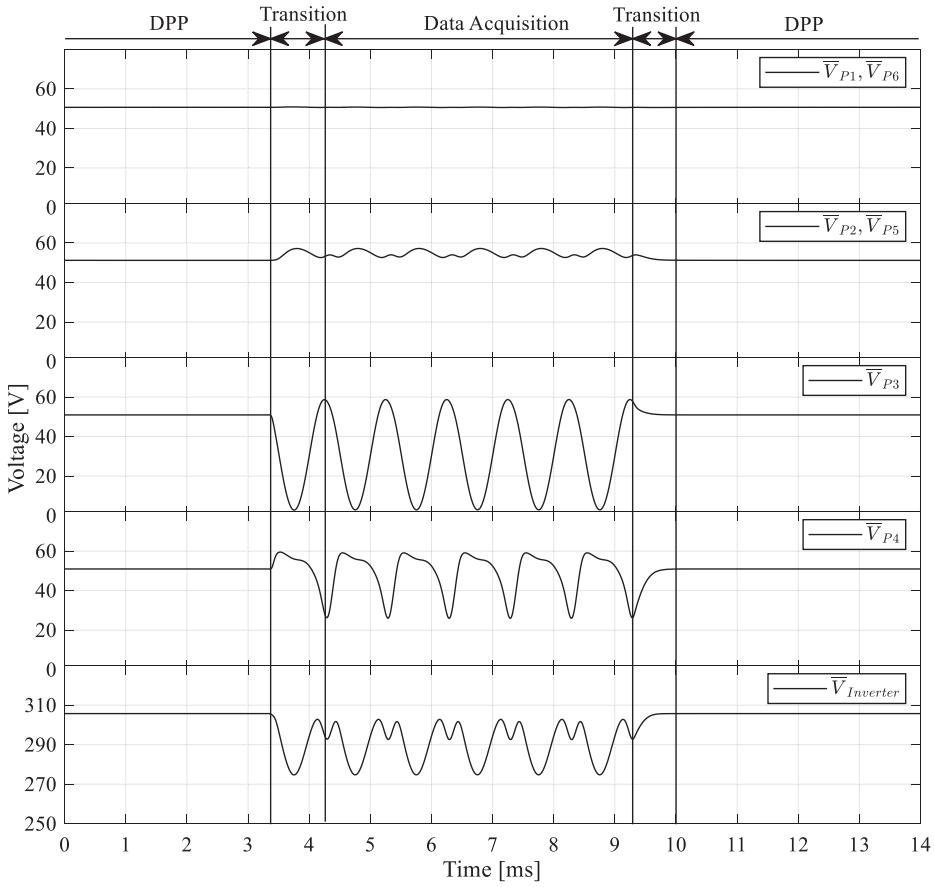


**Fig. 15.** Voltage series.

and $P_4$, such that the voltage of $P_3$ follows a sinusoidal reference signal. The perturbation frequency is 1 kHz. The sampling frequency is 100 kHz. 5 periods of the terminal voltage and current of $P_3$ are recorded. The measurement takes less than 7 ms, including the transition periods.

The current passing through the solar string, as depicted in Fig. 16, is seemingly unaffected by the perturbations local to the panels $P_3$ and $P_4$. The reason is the phase of the perturbed currents, such that the currents are almost anti-parallel, as can be seen in Fig. 16 and in detail in Fig. 7.

Furthermore, the $DAM_1$ and $DAM_5$ impose an active control to $P_1$ and $P_6$, such that the panels follow a constant reference voltage. The $DAM_1$ routes a fraction of the current from $P_2$ to $P_1$ in order to boost the voltage of $P_1$. The same holds for $P_5$ and $P_6$ controlled by $DAM_5$. This leads to seemingly constant current through $P_1$ and $P_6$.

The simulated terminal voltage and current of $P_3$ is used to estimate the intrinsic parameters. The RJGGA algorithm is used to perform the estimation with parameters $\eta_c$ and $\eta_m$ determined in Section 3.6. Tables 2 and 3 summarizes all RJGGA parameter values used throughout the rest of the paper.

Table 4 shows the mean value and the standard deviation of the extracted values of the parameters of 100 executions. Moreover, the percentage errors of the mean values are compared with the parameters in Table 1.

Referring to Figs. 15, 16 and Table 3, the following observations are drawn:

- The perturbation is mostly localized at the panels adjacent to the DAM performing the perturbation. This is because the currents of the perturbed panels are approximately anti-parallel.
- Furthermore, the data acquisition poses negligible disruption to the operation of the central inverter, since the data acquisition period is shorter than the hold-up time of a common central inverter (Kathiresan et al., 2017; Lai et al., 2014).
- The perturbation of the current centred around the $I_{MPP}$ is sufficient for estimating intrinsic parameters describing the single-diode dynamic model.
- The estimation process of the intrinsic parameters converges after 20,000 generations using RJGGA and yields negligible error.

### 4.2. Experimental verification

Several experiments are performed using a DAM protype with commercially available solar panels in controlled and outdoor conditions. The panels are selected within similar power output range for result comparison but with distinct way of achieving MPP.

To test the proposed method, the DAM is tested both on panels achieving MPP at relatively high voltage and low current (commercially available panels based on amorphous silicon technology – a-Si) and panels achieving MPP at relatively low voltage but high current (commercially available solar panels based on crystalline technology, either monocrystalline, m-c-Si, or polycrystalline, p-c-Si). Table 5 summarizes the key information about the tested solar panels.

The group 1 is tested in a controlled conditions at different temperatures. The group 2 is tested in outdoor conditions at different levels of irradiation. The 2 different testing setups are illustrated in Fig. 17.

The testing setup in Fig. 17 consists of a pair of series connected solar panels with a resistive load, driving the panels near the MPP. The tested panels in group 1 are illuminated by 18 industrial reflectors, model Philips QVF137, which gradually heat up the panels. The group 2 is illuminated by the Sun in outdoor conditions. The temperature is monitored by thermocouples connected to digital thermometer BTM-

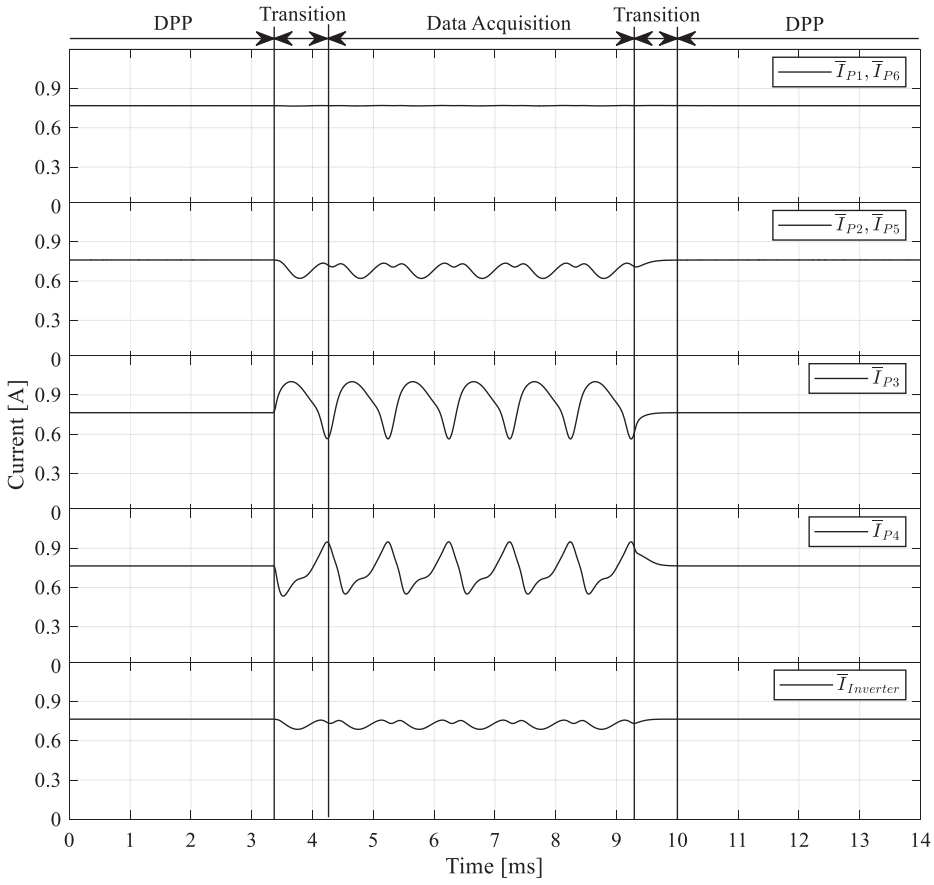


**Fig. 16.** Current series.

**Table 2**
RJGGA parameters.

| *Param.* | *Value* | *Param.* | *Value* |
|---|---|---|---|
| $M$ | 125 | $\eta_c$ | 0.1 |
| $J$ | 25 | $\eta_m$ | 20 |
| $p_j$ | 0.15 | $gen_{max}$ | 20,000 |
| $p_c$ | 0.9 | $N_1$ | 50 |
| $p_m$ | 0.01 | $N_2$ | 500 |

**Table 3**
Search space of the estimated parameters.

| *Param.* | $K_{MIN}$ | $K_{MAX}$ | *Param.* | $K_{MIN}$ | $K_{MAX}$ |
|---|---|---|---|---|---|
| $I_{ph}$ (A) | 0.1 | 5.0 | $R_{sh}$ (Ω) | 100 | 5000 |
| $I_o$ (A) | $1 \times 10^{-12}$ | $1 \times 10^{-3}$ | $C_{sh}$ (μF) | 0.01 | 10 |
| $v_T$ (V) | 1 | 20 | $R_s$ (Ω) | 0.05 | 20 |

**Table 5**
Main properties of the tested solar panels.

| *Panel* | *group 1* | *group 2* |
|---|---|---|
| *manufacturer* | Sungen | Siemens |
| *model* | SG-HN80-GG | SR100 |
| *type* | a-Si | m-c-Si |
| *# of panels* | 4 | 2 |
| $V_{oc}$ *at STC (V)* | 92 | 22 |
| $I_{sc}$ *at STC (A)* | 1.52 | 6.3 |
| $V_{MPP}$ *at STC (V)* | 70 | 17.7 |
| $I_{MPP}$ *at STC (A)* | 1.13 | 5.6 |
| *age (years)* | 20 | 10 |

4208SD forwarding the temperature data to Personal Computer (PC) via UART-USB interface. PC runs a Matlab script, which monitors the temperature and triggers the measurements by sending commands to the Control Module via Ethernet.

Prototypes of a DAM and Control Module are built. The major components used in the DAM prototype are listed in Table 6, Fig. 18

**Table 4**
Mean value, standard deviation, and error of the estimated intrinsic parameters.

| *Param.* | $\mu$ | $\sigma^2$ | $\varepsilon$ (%) | *Param.* | $\mu$ | $\sigma^2$ | $\varepsilon$ (%) |
|---|---|---|---|---|---|---|---|
| $I_{ph}$ *(A)* | 1.00 | $1.79 \times 10^{-6}$ | 0 | $R_{sh}$ (Ω) | 349.9 | $4.12 \times 10^{-3}$ | −0.029 |
| $I_o$ *(A)* | $9.74 \times 10^{-6}$ | $3.24 \times 10^{-9}$ | −2.6 | $C_{sh}$ (μF) | 0.349 | $2.19 \times 10^{-6}$ | −0.289 |
| $v_T$ *(V)* | 5.98 | $1.64 \times 10^{-4}$ | −0.33 | $R_s$ (Ω) | 4.03 | $5.06 \times 10^{-4}$ | 0.75 |

Note:
μ – Mean value.
$\sigma^2$ – Variance.
ε – Percentage error compared with that in Table 1.

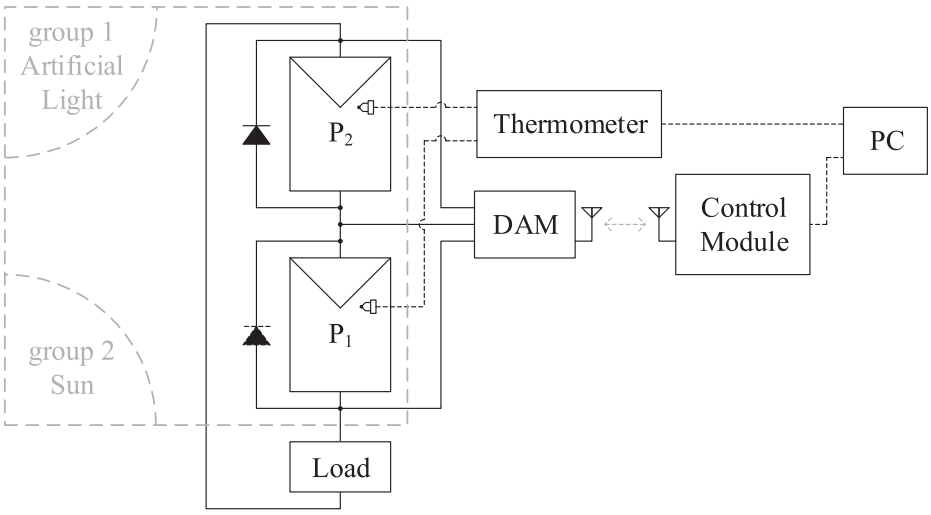


**Fig. 17.** Experimental measurement setup for group 1 and group 2.

**Table 6**
Components Used in the Diagnostic Modules.

| *Part* | *Manufacturer* | *Model number* | *Specification* |
|---|---|---|---|
| *Microcontroller* | STM | STM32F405RG | 168 MHz,12-bit ADC |
| *Op-Amp (V)* | TI | INA826AIDR | 1 MHz, 100 dB CMRR |
| *Op-Amp (I)* | TI | INA240A1 | 400 kHz, 120 dB CMRR |
| *MOSFET* | STM | STP26NM60N | 600 V VDS |
| *Inductor* | Eaton | CTX150-5-52 | 150 µH, 7.7A |
| *Capacitor* | Panasonic | ECQ-E6105KF | 1 µF, 630VDC |
| *Gate driver* | Infineon | IR2110SPBF | up to 500 V, 2A |
| *Wireless Mod.* | NXP | MC1322V | ZigBee |

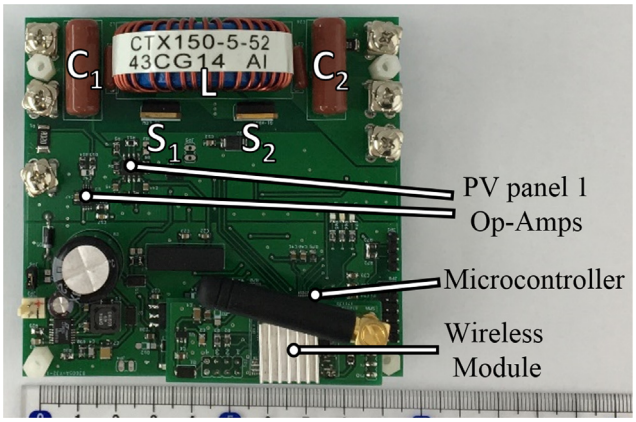


**Fig. 18.** Prototype of Data Acquisition Module.

depicts the developed DAM prototype. The Control Module is based on Raspberry PI 3 model B+.

*4.2.1. Controlled condition tests*

Group 1 consists of 4 solar panels $P_1$ to $P_4$. The panels are tested in pairs in a chamber with controllable temperature. The panels are visually inspected, the following condition is observed:

- $P_1$ and $P_4$ are without visible damage.
- $P_2$ and $P_3$ have cracks stretching across the whole front glass pane.

The testing of the panels is performed as follows:

(1) The lights are turned on, causing the panels to gradually heat-up.
(2) The temperature of the panels is monitored by thermocouples.
(3) The PC triggers the measurement at pre-set temperature.
(4) The DAM is instructed to perturb the panel's voltage and current by the Control Module through ZigBee.
(5) The panel's voltage and current are sampled and sent back to the Control Module.
(6) The Control Module estimates the intrinsic parameters using RJGGA.

The estimation algorithm converges after 20,000 generations, taking approximately 960 s.

The panels $P_1$ to $P_4$ in group 1 are tested under two scenarios.

(a) Standard Testing Conditions (STC) at irradiation 1000 W/m$^2$ and 25 °C.
(b) High temperature measurement at irradiation 1000 W/m$^2$ and 80 °C.

The two scenarios are used to observe temperature dependency of the intrinsic parameters. The panel voltage and current are sampled at 100 kHz.

The measured and pre-processed terminal voltages and currents of panels in group 1 are shown in Fig. 19. The data are measured at STC. The model predicted current, using the estimated parameters obtained by RJGGA, is plotted for comparison.

The estimated intrinsic parameters are listed in Table 7 for the temperature test at 25 °C and 80 °C.

Referring to Fig. 19 and the Table 7, the following observations are drawn:

- DAM can successfully perturb the terminal voltages and currents of a-Si panels and the Control Module can extract the intrinsic parameters with the sampled panel voltage and current.
- Comparison of the estimated parameters between the 2 temperature tests reveals the temperature coefficients of the intrinsic parameters. The $I_{ph}$, $I_O$, $v_T$, $R_s$ and $C_{sh}$ have positive temperature coefficient. The $R_{sh}$ has negative coefficient. This is in accordance with existing literature (Silva et al., 2017).

*4.2.2. Comparative study of controlled condition tests*

The performance of the solar panels is compared with the datasheet values, consisting of the major I-V characteristic points ($V_{oc}$, $I_{sc}$, $V_{MPP}$, $I_{MPP}$) and temperature coefficients (*T. coef.* $V_{oc}$ and $I_{sc}$). Furthermore, the fill-factor (*FF*) is calculated according to (34).

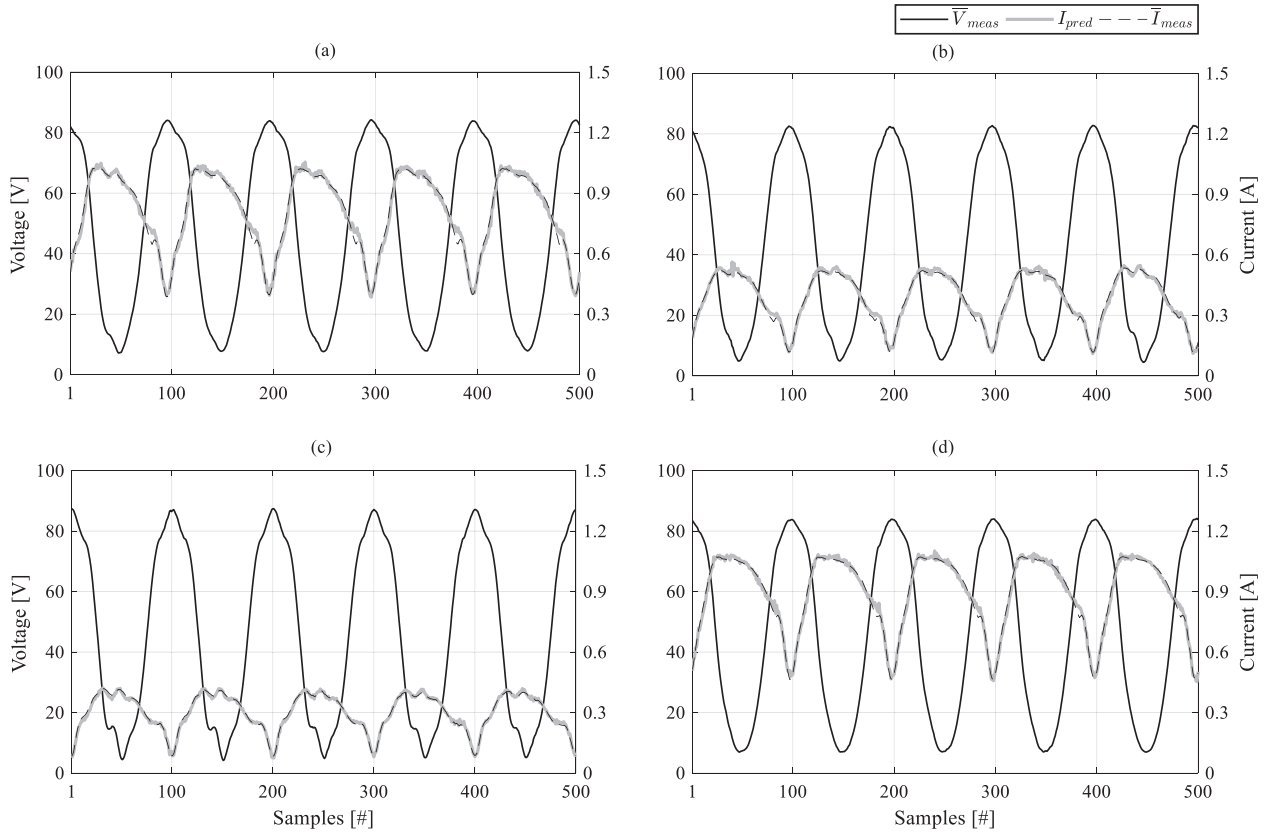


**Fig. 19.** Voltage and current series of (a) $P_1$, (b) $P_2$, (c) $P_3$, (d) $P_4$.

$$FF = \frac{V_{MPP} \times I_{MPP}}{V_{oc} \times I_{sc}} \tag{34}$$

These values are compared with the values from a static I-V characteristic, obtained by the single-diode model by neglecting the effect of the $C_{sh}$ parameter, resulting in single-diode static model. The comparison is summarized in Table 8.

Using the Table 8, the following observations are drawn:

- All solar panels $P_1$ to $P_4$ exhibit signs of aging in form of lower maximum power $P_{MPP}$. The prevalent cause of the power output degradation is significant drop in the $I_{MPP}$.
- The $P_4$ falls within the guaranteed period of average power degradation rate of $-0.92$%/year.
- The $P_1$ shows higher than average power degradation rate of $-1.43$%/year. While both $P_1$ and $P_4$ don't show any visible signs of external damage, $P_1$ is known to be thermally-cycled more often than $P_4$. Thermal-cycling can lead to microscopic cracks within the substrate (Van Mölken et al., 2012), which is a possible cause of higher degradation rate.
- Both $P_2$ and $P_3$ with visible cracks across the front glass pane show abnormally high degradation rates of $-3.46$ and $-3.68$%/year, respectively. The cracks reaching from side-to-side possibly damage the Transparent-Conductive-Oxide (TCO) layer, leading to significant limitation of the passing current.
- The estimated $V_{MPP}$ for $P_3$ and $P_4$ is higher than the value provided in the datasheet. This difference is still within the tolerances, which the datasheet lists as $\pm$ 10% for electrical parameters, such as $V_{MPP}$, and $\pm$ 3% tolerance for power output characteristic.

#### 4.2.3. Outdoor condition tests

Group 2 consists of 2 solar panels $P_5$ and $P_6$. The panels are tested in outdoor conditions at different irradiation levels. The panels are visually inspected, the following condition is observed:

- $P_5$ has slight signs of delamination and air bubbles across 8 solar cells out of 36.
- $P_6$ is without visible damage.

**Table 7**
Estimated intrinsic parameter of panels in group 1.

| *Param.* | *Panel* | | | | | | | |
|---|---|---|---|---|---|---|---|---|
| | $P_1$ | | $P_2$ | | $P_3$ | | $P_4$ | |
| | 25 (°C) | 80 (°C) | 25 (°C) | 80 (°C) | 25 (°C) | 80 (°C) | 25 (°C) | 80 (°C) |
| $I_{ph}$ (A) | 1.01 | 1.08 | 0.53 | 0.60 | 0.41 | 0.44 | 1.08 | 1.15 |
| $I_o$ (A) | $2.11 \times 10^{-8}$ | $1.33 \times 10^{-5}$ | $2.08 \times 10^{-11}$ | $1.50 \times 10^{-9}$ | $1.37 \times 10^{-11}$ | $6.92 \times 10^{-8}$ | $1.62 \times 10^{-9}$ | $9.16 \times 10^{-7}$ |
| $v_T$ (V) | 5.15 | 6.32 | 3.67 | 3.81 | 3.81 | 4.66 | 4.49 | 5.11 |
| $R_{sh}$ (Ω) | 424.63 | 309.32 | 420.75 | 316.66 | 644.44 | 475.73 | 459.42 | 355.69 |
| $C_{sh}$ (μF) | 0.356 | 0.361 | 0.226 | 0.297 | 0.162 | 0.170 | 0.266 | 0.298 |
| $R_s$ (Ω) | 3.33 | 3.50 | 6.52 | 10.64 | 8.43 | 9.32 | 2.03 | 2.39 |

**Table 8**
Comparison of datasheet values with single-diode model prediction for group 1.

| | $P_{MPP}$ (W) | $V_{oc}$ (V) | $I_{sc}$ (A) | $V_{MPP}$ (V) | $I_{MPP}$ (A) | T. coef. $V_{oc}$ (%/K) | T. coef. $I_{sc}$ (%/K) | FF (–) |
|---|---|---|---|---|---|---|---|---|
| Datasheet | 80.00 | 92.00 | 1.39 | 70.50 | 1.13 | −0.36 | 0.13 | 0.62 |
| $P_1$ | 57.08 | 89.86 | 1.00 | 72.78 | 0.78 | −0.40 | 0.11 | 0.63 |
| $P_2$ | 24.57 | 86.14 | 0.52 | 70.63 | 0.34 | −0.26 | 0.19 | 0.54 |
| $P_3$ | 21.06 | 90.31 | 0.40 | 74.95 | 0.28 | −0.38 | 0.12 | 0.57 |
| $P_4$ | 65.23 | 90.32 | 1.07 | 74.96 | 0.87 | −0.39 | 0.11 | 0.67 |

The testing of the panels is performed as follows:

(1) The panels are placed facing the Sun until the temperature stabilizes.
(2) The irradiation is measured by a short-circuit current of a calibrated reference solar cell.
(3) The temperature of the panels is monitored by thermocouples.
(4) The DAM is instructed to perturb the panel's voltage and current by the Control Module through ZigBee.
(5) The panel's voltage and current are sampled and sent back to the Control Module.
(6) The Control Module estimates the intrinsic parameters using RJGGA.

The panels are tested under two scenarios:

(a) Panels are facing the Sun at angle 0° (perpendicular to incoming light), the irradiation is 750 W/m$^2$ and the temperature 50 °C.
(b) Panels are tilted by approximately 48°, the irradiation is 500 W/m$^2$ and the temperature 50 °C.

The two scenarios are used to observe the irradiation dependency of the intrinsic parameters. The panel voltage and current are sampled at 100 kHz.

The measured and pre-processed terminal voltages and currents of panels $P_5$ and $P_6$ are shown in the Fig. 20. The plotted data are measured at the irradiation of 750 W/m$^2$. The model predicted current using the estimated parameters is plotted for comparison.

The estimated intrinsic parameters of $P_5$ and $P_6$ are listed in Table 9. Using the Fig. 20 and Table 9, the following observations are drawn:

- DAM can successfully perturb the terminal voltages and currents of c-Si panels and the Control Module can extract the intrinsic parameters with the sampled panel voltages and currents.
- Comparison of the estimated parameters between the 2 different irradiation tests reveal the irradiation coefficients of the intrinsic parameters. The $I_{ph}$, $I_0$ and $C_{sh}$ have positive irradiation coefficient, while $R_{sh}$ has negative coefficient.
- The change in $R_s$ has positive irradiation coefficient. The literature (Silva et al., 2017) reports marginally negative coefficient. While (Silva et al., 2017) investigates static I-V characteristics, this work estimates the intrinsic parameters from large-signal AC characteristic. Therefore, the discrepancy in findings may imply a non-linearity of the PV panel impedance under AC operation. Further research will be dedicated to interpreting $R_s$ under static and dynamic excitation.

**Table 9**
Estimated values of the intrinsic parameters of group 2.

| Param. | Panel | | | |
|---|---|---|---|---|
| | $P_5$ | | $P_6$ | |
| | 500 (W/m$^2$) | 750 (W/m$^2$) | 500 (W/m$^2$) | 750 (W/m$^2$) |
| $I_{ph}$ (A) | 2.99 | 4.47 | 3.11 | 4.66 |
| $I_0$ (A) | $1.05 \times 10^{-5}$ | $2.01 \times 10^{-5}$ | $2.85 \times 10^{-6}$ | $8.12 \times 10^{-6}$ |
| $v_T$ (V) | 1.55 | 1.56 | 1.40 | 1.46 |
| $R_{sh}$ (Ω) | 313.70 | 304.34 | 201.43 | 194.02 |
| $C_{sh}$ (μF) | 0.71 | 1.09 | 0.96 | 1.13 |
| $R_s$ (Ω) | 0.10 | 0.27 | 0.13 | 0.24 |

#### 4.2.4. Comparative study of outdoor condition tests

The comparative study between the values reported in the datasheet and the values obtained by the single-diode model is performed similarly as outlined in Section 4.2.2. Due to outdoor conditions being different from the STC values provided in the datasheet, the datasheet values are recalculated to the outdoor conditions, irradiation 750 W/m$^2$ and temperature 50 °C according to (IEC 60891 Ed.2, 2009).

Furthermore, the irradiation dependency of $V_{oc}$ and $I_{sc}$ are not included in the datasheet, therefore they are *interpolated* from the I-V reference characteristics in the datasheet. The comparison is summarized in Table 10.

Using the Table 10, the following observations are drawn:

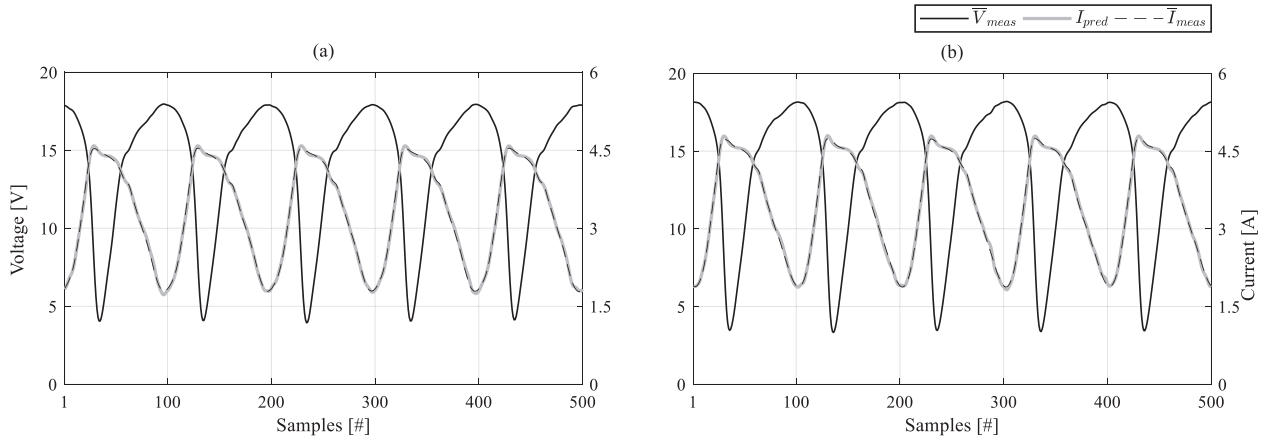


**Fig. 20.** Voltage and current series of (a) $P_5$ and (b) $P_6$.

**Table 10**
Comparison of datasheet values with single-diode model prediction for group 2.

| | $P_{MPP}$ (W) | $V_{oc}$ (V) | $I_{sc}$ (A) | $V_{MPP}$ (V) | $I_{MPP}$ (A) | G. coef. $V_{oc}$ (%/(W/m$_2$)) | G. coef. $I_{sc}$ (%/(W/m$_2$)) | FF (–) |
|---|---|---|---|---|---|---|---|---|
| *Datasheet* | 68.78 | 19.62 | 4.97 | 15.22 | 4.52 | *0.0114* | *0.0974* | 0.70 |
| $P_5$ | 57.76 | 19.18 | 4.46 | 14.58 | 3.96 | 0.0129 | 0.1326 | 0.67 |
| $P_6$ | 61.74 | 19.32 | 4.65 | 14.88 | 4.14 | 0.0123 | 0.1325 | 0.68 |

- Both solar panels $P_5$ and $P_6$ exhibit signs of power degradation in form of lower maximum power output. The main cause is the change in the $I_{MPP}$, similarly to test group 1.
- The average power degradation rate for $P_5$ is $-0.34$%/year, the $P_6$ attains the rate of $-0.75$%/year. Compared to group 1, the group 2 has been stored at stable room temperature and humidity, which prevents the panel from incurring damage.
- The panel $P_5$, with slight but visible degradation in form of delamination, is observed to have lower power output compared to panel $P_6$ of the same age but without visible degradation.

## 5. Conclusion

A novel method for data acquisition of the photovoltaic panel's dynamic I-V characteristic under operation and subsequent estimation of the intrinsic parameters is presented. The method outcompetes the common identification methods by acquiring the data online, without directly impacting the power generation process. Furthermore, compared to other approaches based on single-diode model, the identification process yields both static and dynamic parameters from a single measurement.

The simulation results are experimentally verified under controlled and outdoor conditions on amorphous- and crystalline-silicon solar panel technologies. The testing shows a Differential Power Processing module with altered control software is capable of performing large-signal voltage perturbations to acquire dynamic I-V characteristic of two photovoltaic panels connected in series.

The data acquisition period of 7 ms is shorter than a hold-up-time of a common central inverter, therefore it poses a negligible disruption to the power generation process.

Furthermore, the perturbation is mostly localized at the panels adjacent to the module performing the perturbation process, due to the perturbed currents being almost anti-parallel, further minimizing the impact on the power generation process.

Two evolutionary algorithms are utilized to investigate the difficulty of the proposed parameter identification problem of nonlinear model from the acquired time series. The *m*-PSO, which has been successfully used for linear model identification tasks, shows presence of multiple local optima. The RJGGA with adjustable exploration and exploitation rate for single-objective optimization shows the problem requires high exploration rate to obtain a consistent convergence. The intrinsic parameter estimation of the dynamic single-diode model using RJGGA converges after 20,000 generations with the population of 125 chromosomes.

Experimental testing of 6 solar panels shows degradation rates correlate with observed damage. A 2 a-Si panels without physical damage are diagnosed with degradation rates of $-0.92$ and $-1.43$%/year in power output. A 2 a-Si panels with cracks across the front glass panel are diagnosed with degradation rates of $-3.46$ and $-3.68$%/year. A 2 m-c-Si panels are diagnosed $-0.34$%/year and $-0.75$%/year, where the latter case has 8 cells out of 36 affected by slight delamination.

The estimated intrinsic capacitance has positive correlation with the observed degradation, establishing a possible indicator of the panel's health condition. Furthermore, the static parameters estimated from the dynamic perturbations show the major cause of the power output degradation is the decline in the short-circuit and MPP current.

## Declaration of Competing Interest

The authors declare that they have no known competing financial interests or personal relationships that could have appeared to influence the work reported in this paper.

## Acknowledgement

The work was supported by a grant from the Innovation Fund Denmark through the project APETT with no.: 6154-00010B.

## References

Ahadi, A., Ghadimi, N., Mirabbasi, D., 2014. Reliability assessment for components of large scale photovoltaic systems. J. Power Sources. https://doi.org/10.1016/j.jpowsour.2014.04.041.
Askarzadeh, A., Rezazadeh, A., 2011. Optimization of PEMFC model parameters with a modified particle swarm optimization. Int J. Energy Res 10.1002/er.1787.
Cotfas, D.T., Cotfas, P.A., Kaplanis, S., 2016. Methods and techniques to determine the dynamic parameters of solar cells: review. Renew Sustain. Energy Rev. https://doi.org/10.1016/j.rser.2016.03.051.
Crepinsek, M., Liu, S.-H., Mernik, M., 2011. Exploration and exploitation in evolutionary algorithms: a survey. ACM Comput. Surv. https://doi.org/10.1145/2480741.2480752.
Deb, K., 2011. Multi-objective optimisation using evolutionary algorithms: an introduction. In: Multi-Objective Evolutionary Optimisation for Product Design and Manufacturing, https://doi.org/10.1007/978-0-85729-652-8_1.
Deline, C., Nick, D., Jordna, D., 2016. Progress & Frontiers in PV Performance. Las Vegas, Nevada.
Garaj, M., Hong, K.Y., Shu-Hung Chung, H., Zhou, J., Lo, A.W.L., 2019. Photovoltaic panel health diagnostic system for solar power plants. Conference Proceedings – IEEE Applied Power Electronics Conference and Exposition – APEC. https://doi.org/10.1109/APEC.2019.8721839.
Humada, A.M., Hojabri, M., Mekhilef, S., Hamada, H.M., 2016. Solar cell parameters extraction based on single and double-diode models: a review. Renew Sustain. Energy Rev. https://doi.org/10.1016/j.rser.2015.11.051.
IEC 60891 Ed.2, 2009. Photovoltaic devices - Procedures for temperature and irradiance corrections to measured I-V characteristics. Photovolt. Devices.
Ishaque, K., Salam, Z., Taheri, H., Syafaruddin, 2011. Modeling and simulation of photovoltaic (PV) system during partial shading based on a two-diode model. Model. Pract. Theory Simul 10.1016/j.simpat.2011.04.005.
Ishibuchi, H., Nojima, Y., Tsutomu Doi, 2006. Comparison between single-objective and multi-objective genetic algorithms: performance comparison and performance measures. https://doi.org/10.1109/cec.2006.1688438.
Kathiresan, R., Das, P., Reindl, T., Panda, S.K., 2017. A novel ZVS DC-DC full-bridge converter with hold-up time operation. IEEE Trans. Ind. Electron. https://doi.org/10.1109/TIE.2017.2674583.
Kim, K.A., Xu, C., Jin, L., Krein, P.T., 2013. A dynamic photovoltaic model incorporating capacitive and reverse-bias characteristics. IEEE J. Photovolt. https://doi.org/10.1109/JPHOTOV.2013.2276483.
Lai, Y.S., Su, Z.J., Chen, W.S., 2014. New hybrid control technique to improve light load efficiency while meeting the hold-up time requirement for two-stage server power. IEEE Trans. Power Electron. https://doi.org/10.1109/TPEL.2013.2283747.
Lim, L.H.I., Ye, Z., Yang, D., 2015. Non-contact measurement of POA irradiance and cell temperature for PV systems. In: IECON 2015 – 41st Annual Conference of the IEEE Industrial Electronics Society, https://doi.org/10.1109/IECON.2015.7392130.
Ma, X., Huang, W.-H., Schnabel, E., Kohl, M., Brynjarsdottir, J., Braid, J.L., French, R.H., 2019. Data-driven I-V feature extraction for photovoltaic modules. IEEE J. Photovolt. https://doi.org/10.1109/jphotov.2019.2928477.
Nawaz Ripon, K.S., Kwong, S., Man, K.F., 2007. A real-coding jumping gene genetic algorithm (RJGGA) for multiobjective optimization. Inf. Sci. (Ny). https://doi.org/10.1016/j.ins.2006.07.019.
Ono, I., Kobayashi, S., Yoshida, K., 2000. Optimal lens design by real-coded genetic algorithms using UNDX. Comput. Methods Appl. Mech. Eng. https://doi.org/10.1016/S0045-7825(99)00398-9.
Panigrahi, J., Vandana, Singh, R., Batra, N., Gope, J., Sharma, M., Pathi, P., Srivastava, S.K., Rauthan, C.M.S., Singh, P.K., 2016. Impedance spectroscopy of crystalline silicon solar cell: observation of negative capacitance. Sol. Energy. https://doi.org/10.1016/j.solener.2016.06.041.
Patel, H., Agarwal, V., 2008. MATLAB-based modeling to study the effects of partial shading on PV array characteristics. IEEE Trans. Energy Convers. https://doi.org/10.

1109/TEC.2007.914308.
Qin, S., Cady, S.T., Dominguez-Garcia, A.D., Pilawa-Podgurski, R.C.N., 2015. A distributed approach to maximum power point tracking for photovoltaic submodule differential power processing. IEEE Trans. Power Electron. https://doi.org/10.1109/TPEL.2014.2330335.
Sangwongwanich, A., Yang, Y., Sera, D., Blaabjerg, F., 2018. Lifetime evaluation of grid-connected PV inverters considering panel degradation rates and installation sites. IEEE Trans. Power Electron. https://doi.org/10.1109/TPEL.2017.2678169.
Shenoy, P.S., Kim, K.A., Johnson, B.B., Krein, P.T., 2013. Differential power processing for increased energy production and reliability of photovoltaic systems. IEEE Trans. Power Electron. https://doi.org/10.1109/TPEL.2012.2211082.
Silva, E.A., Bradaschia, F., Cavalcanti, M.C., Nascimento, A.J., Michels, L., Pietta, L.P., 2017. An eight-parameter adaptive model for the single diode equivalent circuit based on the photovoltaic module's physics. IEEE J. Photovolt. https://doi.org/10.1109/JPHOTOV.2017.2703778.
Srinivas, M., Patnaik, L.M., 1994. Adaptive probabilities of crossover and mutation in genetic algorithms. IEEE Trans. Syst. Man Cybern. https://doi.org/10.1109/21.286385.
Suskis, P., Galkin, I., 2013. Enhanced photovoltaic panel model for MATLAB-simulink environment considering solar cell junction capacitance. In: IECON Proceedings (Industrial Electronics Conference), https://doi.org/10.1109/IECON.2013.6699374.
Van Mölken, J.I., Yusufoğlu, U.A., Safiei, A., Windgassen, H., Khandelwal, R., Pletzer, T.M., Kurza, H., 2012. Impact of micro-cracks on the degradation of solar cell performance based on two-diode model parameters. Energy Procedia. https://doi.org/10.1016/j.egypro.2012.07.046.
Wang, W., Chung, H.S.H., Zhang, J., 2014. Near-real-time parameter estimation of an electrical battery model with multiple time constants and SoC-dependent capacitance. In: 2014 IEEE Energy Conversion Congress and Exposition, ECCE 2014, https://doi.org/10.1109/ECCE.2014.6953942.
Wang, W., Liu, A.C.F., Chung, H.S.H., Lau, R.W.H., Zhang, J., Lo, A.W.L., 2016. Fault diagnosis of photovoltaic panels using dynamic current-voltage characteristics. IEEE Trans. Power Electron. https://doi.org/10.1109/TPEL.2015.2424079.
Yahya-Khotbehsara, A., Shahhoseini, A., 2018. A fast modeling of the double-diode model for PV modules using combined analytical and numerical approach. Sol. Energy. https://doi.org/10.1016/j.solener.2018.01.047.